Application and Development of Aircraft Flyover Measurements in China

Haoyuan Dong , Cheng Wei Lee , Yuqi Zhou , Wei Ma *

Posted Date: 18 March 2026

doi: 10.20944/preprints202603.1424.v1

Keywords: aircraft flyover measurements; microphone array; large civil aircraft; computer vision; aircraft trajectory determination; sound source localization

 doi:10.20944/preprints202603.1424.v1

Article

Application and Development of Aircraft Flyover Measurements in China

Haoyuan Dong, Cheng Wei Lee, Yuqi Zhou and Wei Ma *

School of Aeronautics and Astronautics, Shanghai Jiao Tong University, 800 Dongchuan Road, Shanghai 200240, China

* Correspondence: mawei@sjtu.edu.cn

Abstract

Aircraft flyover measurements are used to record the acoustic pressure signals generated by large civil aircraft as they fly over a large-scale microphone array deployed on the ground, thereby obtaining the spatial distribution of aircraft airframe noise and providing technical support for aircraft noise reduction. Aircraft flyover measurements have been widely applied in the research and development of numerous large civil aircraft in Europe and North America since the 1990s. In recent years, aircraft flyover measurements have also been extensively adopted in China, particularly with the rapid development of C919, China's large civil aircraft. Computer vision techniques have also been applied to microphone position calibration and aircraft trajectory determination in measurements, which has effectively improved measurement efficiency and accuracy. This paper presents an integrated procedure for aircraft flyover measurements of large civil aircraft in China, including microphone array design, installation, and calibration, noise acquisition system setup and data acquisition, aircraft trajectory determination, and data processing.

Keywords: aircraft flyover measurements; microphone array; large civil aircraft; computer vision; aircraft trajectory determination; sound source localization

1. Introduction

With the development of the civil aviation industry, the impacts of aircraft noise on communities surrounding airports and on public health have become increasingly prominent. In response, the International Civil Aviation Organization (ICAO) and national civil aviation authorities have successively established explicit noise limits for aircraft through airworthiness regulations [1,2]. Effective aircraft noise control generally requires a clear understanding of the spatial distribution of airframe noise sources. Aircraft flyover measurements use a large-scale microphone array deployed on the ground to record the sound pressure signals generated as a large civil aircraft passes overhead, thereby allowing the spatial distribution of airframe noise sources to be identified and providing technical support for aircraft noise reduction.

The widespread application of aircraft flyover measurements in the aviation field can be traced back to the pioneering work of Michel's team at the German Aerospace Center (DLR) in the 1990s [3–5]. They were the first to apply large-aperture microphone arrays to outdoor aircraft flyover measurements, achieving spatial localization of the major noise sources under real flight conditions. Since then, aircraft flyover measurements have been widely used in the development of mainstream aircraft types in Europe and North America, and dedicated testing frameworks and analysis methods have gradually been developed for different aircraft configurations. From 2001 to 2005, under the Quiet Technology Demonstrator (QTD) program, the National Aeronautics and Space Administration (NASA) and Boeing conducted multiple flyover noise test campaigns on the B777 [6,7]. By combining far-field ground microphones with large-aperture phased microphone arrays, they identified and compared the noise contributions of key components such as the landing gear and high-lift system. In 2002, DLR and French Aerospace Lab (ONERA) jointly conducted multiple

 doi:10.20944/preprints202603.1424.v1

flyover noise tests on the A340 using a 16m×16m nested array [8]. The results showed that flyover measurements could identify the locations of the dominant noise sources with relatively good stability, whereas the estimated source strengths were strongly affected by test conditions and showed relatively weak consistency. In 2004, DLR performed a dedicated flyover noise experiment on the A319 for the validation of airframe noise prediction methods and the establishment of a noise database, providing foundational data support for subsequent noise-reduction studies [9]. In 2012, Bombardier Aerospace and the acoustics group at the Université de Sherbrooke conducted a five-day aircraft flyover measurement campaign [10]. By deploying a large-aperture microphone array and two high-definition cameras, they recorded the noise and trajectory data from multiple CRJ200 flyovers, thereby verifying the repeatability of a synchronized noise-and-trajectory acquisition method under real airport operating conditions. In 2018, NASA performed research on the B737MAX and systematically described the experimental procedures of aircraft flyover measurements, extending its application to full-scale flight validation of noise-reduction components [11]. From 2018 to 2022, DLR carried out a series of flyover noise tests using its research aircraft ATRA (an Airbus A320-232) [12,13]. During these campaigns, measurement procedure was further optimized through new aircraft trajectory determination methods and the adoption of a large multi-arm spiral array. In 2020, NASA and Boeing conducted aircraft flyover measurements on the B787. The study provided a systematic description of engineering aspects including array deployment, microphone position calibration, and the synchronized acquisition of acoustic measurements and aircraft trajectory data [14].

In China, aircraft flyover measurements were initiated during the development of the C909 regional aircraft (formerly ARJ21), laying an important practical and technical foundation for subsequent research. From 2012 to 2013, Chen Tao et al. conducted flyover measurements on the C909 under various flight conditions and analyzed the corresponding microphone array data [15–17]. Their work characterized the noise contributions of key components, especially the landing gear and high-lift systems, under different operating conditions, and provided important support for later noise-reduction design and engineering flight-test validation.

In recent years, the development of China's large civil aircraft C919 has made rapid progress. The aircraft completed its maiden flight on May 5, 2017, received its Type Certificate from the Civil Aviation Administration of China (CAAC) on Sept. 29, 2022, was first delivered on Dec. 9, 2022, and successfully entered commercial service with its first commercial flight on May 28, 2023. Aircraft flyover measurements were widely applied during the development of the C919. More recently, advanced computer vision techniques have been introduced into such measurements for microphone position calibration and aircraft trajectory determination, thereby improving both efficiency and accuracy.

This paper is organized as follows. Section 0 outlines the overall procedure of aircraft flyover measurements. Section 0 presents the design, installation, and calibration of the microphone array. Section 0 describes the setup of the noise acquisition system and the acquisition of flyover noise data. Section 0 introduces the method for aircraft trajectory determination. Section 0 presents the data processing procedure and its application to sound source localization. Finally, conclusions are given in Section 0.

2. Overall Procedure of Aircraft Flyover Measurements

In practical full-scale flyover tests, the overall procedure of aircraft flyover measurements for domestically developed large civil aircraft can be divided into four main stages, as illustrated in Figure 1, including microphone array design, installation, and calibration, noise acquisition system setup and data acquisition, aircraft trajectory determination, and data processing.

 doi:10.20944/preprints202603.1424.v1

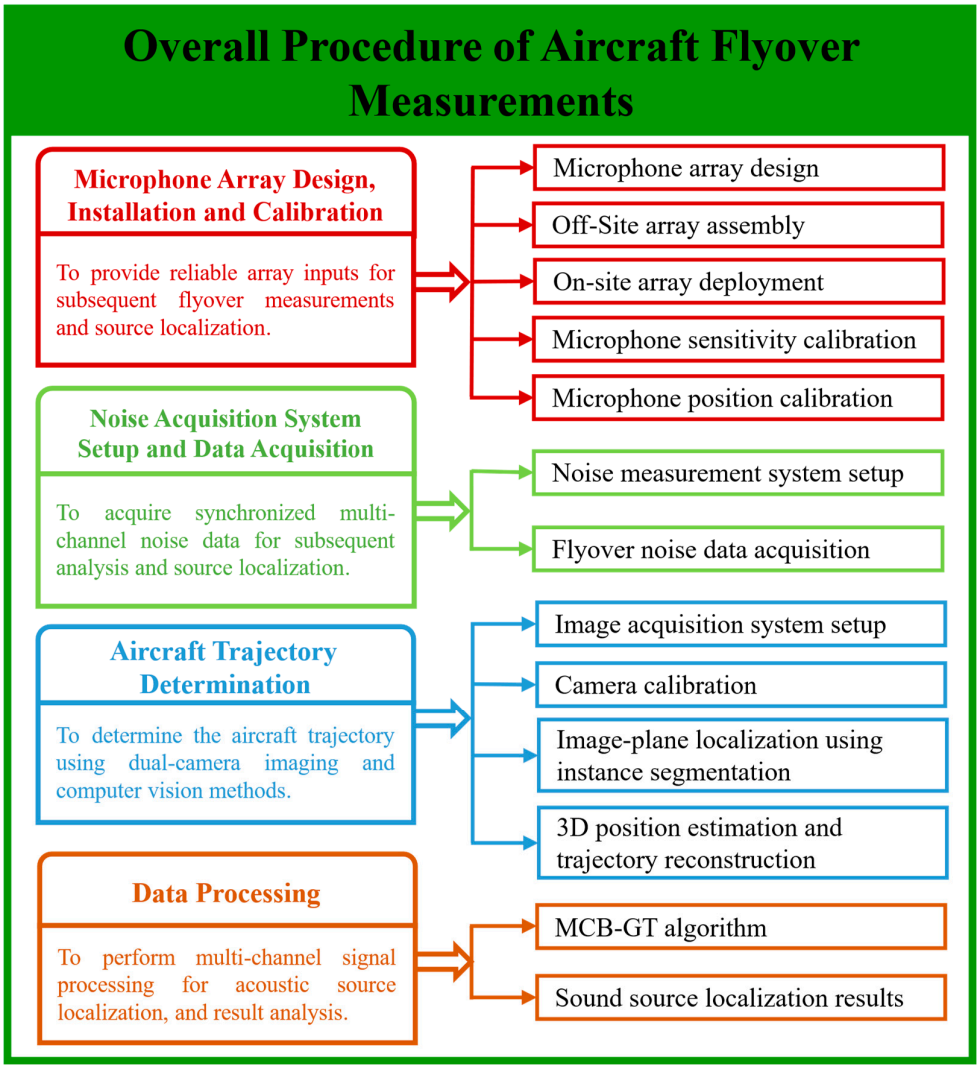

Figure 1. Overall procedure of aircraft flyover measurements.

The first stage involves microphone array design, off-site assembly, on-site deployment, microphone sensitivity calibration and position calibration, thereby providing reliable array inputs for subsequent sound source localization. After the array preparation is completed, a flyover noise acquisition system is established to synchronously record multi-channel array noise data during the aircraft flyover. Meanwhile, aircraft trajectory information is obtained using a dual-camera system combined with advanced computer vision algorithms. Finally, the acquired noise data, array coordinates, and trajectory information are integrated for data processing and sound source localization. The technical details of each stage are presented in the following sections.

3. Microphone Array Design, Installation and Calibration

3.1 Microphone Array Design

The microphone array used for aircraft flyover measurements must support broadband source localization. At low frequencies, spatial resolution is governed primarily by array aperture, which calls for a large aperture. At mid- and high-frequency ranges, accurate source localization and reliable beamforming require a higher spatial sampling density and a more uniform planar sensor distribution [18]. In practice, the number of available acquisition channels and the constraints of field deployment make it difficult for a single array geometry to satisfy these competing requirements

 doi:10.20944/preprints202603.1424.v1

across the full frequency range. For this reason, a nested array consisting of an inner subarray and an outer subarray was adopted in this study [19]. The overall array layout is shown in Figure 2.

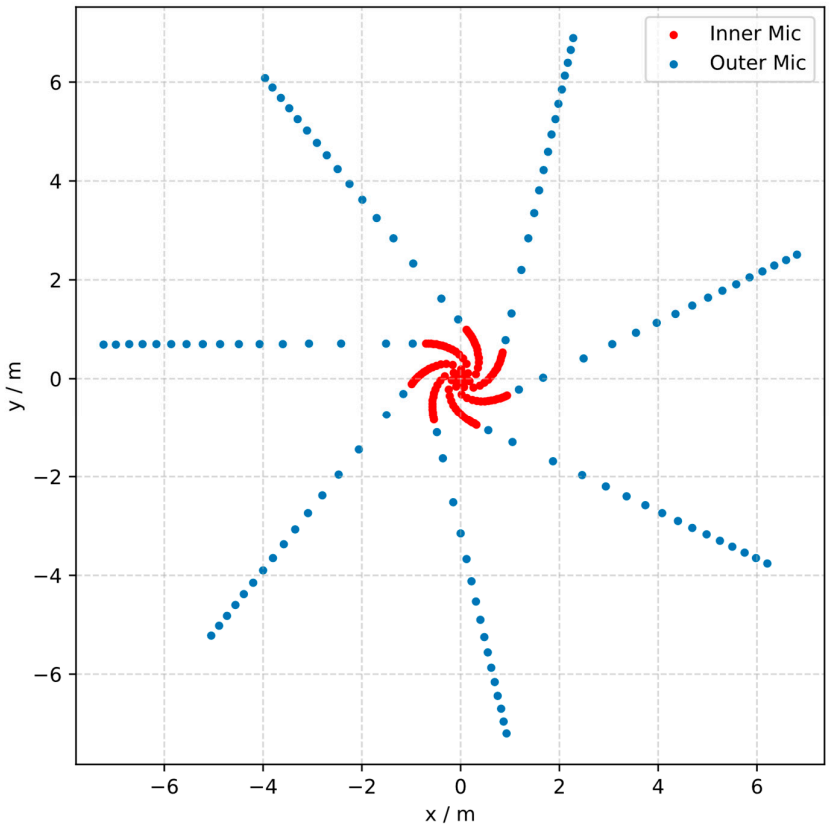

Figure 2. Microphone array design.

The inner subarray is intended to provide the spatial sampling density required for source localization at mid- and high-frequency ranges. It therefore adopts a multi-arm spiral geometry [18], with an effective aperture of 2 m. The subarray comprises seven spiral arms, each carrying 16 microphones, giving a total of 112 channels. The outer subarray is introduced to increase the effective aperture and thus improve source discrimination at low frequencies. To simplify field deployment of the large array, the outer subarray is arranged as a straight-arm layout, with each arm extending outward along the directions defined by the inner subarray. Based on the resolution requirement at the lowest frequency of interest, the effective aperture of the outer subarray is set to 14.5 m. Each arm contains 16 microphones, again giving a total of 112 channels.

By combining an inner multi-arm spiral subarray with an outer straight-arm subarray, the proposed array achieves broadband source localization while remaining practical for large-scale field deployment

3.2. Off-Site Array Assembly

Preparation of the large microphone array was divided into two stages: off-site assembly and on-site deployment. This approach improved deployment efficiency and reduced installation errors associated with complex on-site operations. The off-site stage includes equipment installation, microphone mounting and cabling, and marking the positions of individual modules. This enables transportable array modules to be prepared in advance and to deploy them rapidly at the test site, thereby reducing the effort required for on-site setup during flyover measurements.

The inner subarray is constructed as an integrated unit on a circular platform 2.2 m in diameter. The platform consists of a thick wooden base overlaid with an aluminum plate of the same size to

 doi:10.20944/preprints202603.1424.v1

provide sufficient structural rigidity and to reduce the influence of changing ground conditions on measurement consistency. After the origin and coordinate axes are established, the planar coordinate system and microphone locations are marked on the platform surface, followed by microphone installation, cabling, and fastening. The assembled inner subarray is shown in Figure 3. This integrated design helps maintain positional stability of the microphones during transportation and field deployment.

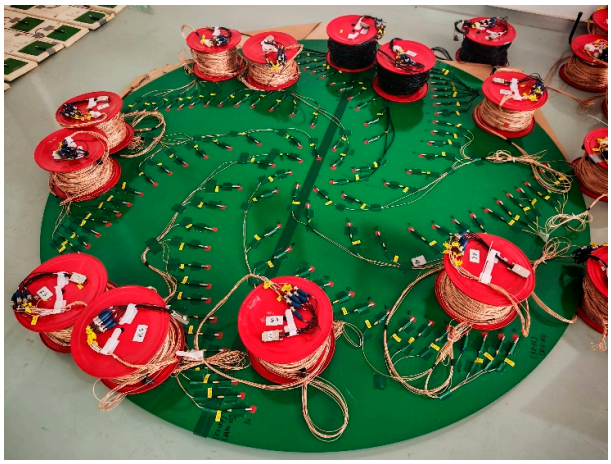

Figure 3. Assembled configuration of the inner subarray.

The outer subarray is constructed as a modular straight-arm layout. To facilitate transportation and rapid field deployment, each arm is divided into three independent modules. Every module consists of a wooden base of a specified length, overlaid with a standardized aluminum plate used as the reflecting surface, with the plate center taken as the microphone location. Once the microphones are installed, cabling and fixation are completed for each module, and the corresponding deployment positions are marked in advance. The assembled outer subarray is shown in Figure 4. This modular design helps streamline on-site deployment of the large microphone array.

Figure 4. Assembled configuration of the outer subarray.

3.3. On-Site Array Deployment

After the test window has been established, on-site deployment of the array is carried out, including module placement, cable connection, and channel verification. The inner platform is positioned first, with its geometric center aligned with the center of the measurement area. The outer modules are then arranged in the predefined order so that they extend outward along the tangential directions defined by the arms of the inner subarray, forming the full nested array. A final channel check is carried out to confirm normal acquisition on all microphone channels, correct channel numbering and mapping, and reliable cable connections. The deployed array is shown in Figure 5.

 doi:10.20944/preprints202603.1424.v1

Figure 5. On-site deployment of the array.

3.4. Microphone Sensitivity Calibration

Each microphone channel was calibrated individually using a standard acoustic calibrator to ensure a consistent amplitude response across the array. The channel responses were recorded under identical excitation conditions, and the resulting sensitivity correction factors were used for subsequent amplitude correction.

3.5. Microphone Position Calibration

Errors in microphone position calibration can degrade array phase coherence and thereby bias source localization. Direct measurement of individual microphone positions using high-precision surveying equipment can provide accurate coordinates, but the procedure is labor-intensive, time-consuming, and difficult to implement efficiently under field conditions. This makes it impractical for the rapid deployment of large outdoor arrays. To address this limitation, a computer-vision-based method was developed for microphone position calibration. The procedure includes array image acquisition, distortion correction and perspective rectification, reflector detection and image localization, and microphone coordinate estimation.

The inner subarray is constructed as an integrated unit, and its geometry is therefore relatively stable. Position calibration is accordingly applied only to the microphones in the outer subarray. The overall procedure is shown in Figure 6. A high-resolution camera is first used to capture an image of the full array. The image is then corrected for lens distortion and rectified by perspective transformation to obtain a uniformly scaled plan view. The reflector plates are identified based on their color and shape, and their centers are taken as the image coordinates of the microphones. These image coordinates are then mapped to the planar array coordinate system to determine the calibrated positions of all microphones in the outer subarray.

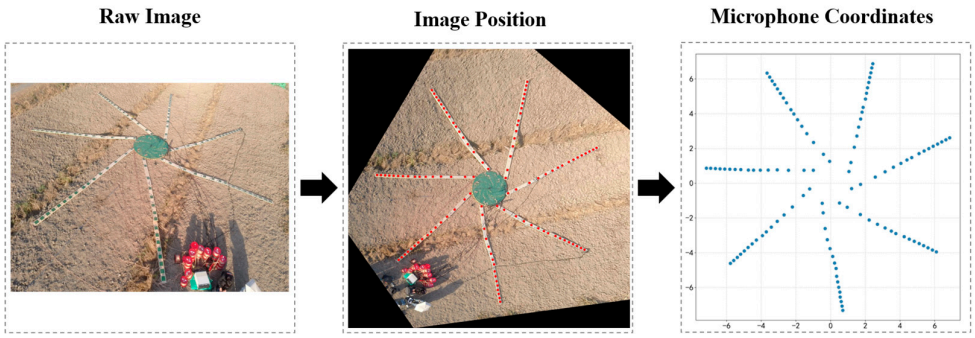

Figure 6. Procedure of Microphones Position Calibration for the outer subarray.

The proposed calibration method was assessed by comparison with reference coordinates obtained from high-precision surveying of the microphones in the outer subarray. The mean error

 doi:10.20944/preprints202603.1424.v1

between the surveyed coordinates and the vision-based calibration results was 0.076 m, which is approximately 0.52% of the array aperture. According to previous studies [20], positional errors at this level are not expected to significantly affect source localization performance in aircraft flyover measurements. In view of the much greater operational complexity and time required for direct measurement—typically several to tens of times greater than that of the proposed method—the computer-vision-based approach is better suited to large-scale field applications.

4. Noise Acquisition System Setup and Data Acquisition

4.1. Noise Acquisition System Setup

The acoustic measurement system comprises microphones, a data acquisition unit, and a host computer. The array is equipped with 224 PCB 130F22 microphones for multichannel pressure recording. These microphones provide adequate frequency response over the frequency range of interest. Data acquisition is implemented on a National Instruments (NI) PXIe platform consisting of a PXIe-8880 controller, fourteen PXIe-4497 modules, and an 18-slot PXIe-1085 chassis. Together, these components provide synchronized acquisition across 224 channels and support high-speed data transfer.

4.2. Flyover Noise Data Acquisition

Noise acquisition system is started shortly before the aircraft approaches the array and continuously records all microphone channels synchronously. Global Positioning System (GPS) pulse signals are used for triggering, and absolute timestamps are recorded simultaneously, allowing the noise data to remain time-aligned across channels and allowing direct temporal alignment with the reconstructed trajectory. The flyover noise data acquisition process is shown in Figure 7.

Figure 7. Flyover Noise Data Acquisition.

 doi:10.20944/preprints202603.1424.v1

5. Aircraft Trajectory Determination

The aircraft position and velocity during the flyover are key inputs to sound source localization in aircraft flyover measurements, and their accuracy directly affects the reliability of the resulting acoustic images. Early studies proposed a dual-camera-based method for determining the aircraft trajectory and demonstrated its feasibility [10]. However, limited by the algorithms available at the time, most of these studies relied on conventional target detection methods. With recent advances in computer vision, more sophisticated visual techniques can now be incorporated into trajectory determination. Building on these earlier efforts, this study proposes a trajectory determination method based on a dual-camera system and instance segmentation. The overall procedure includes image acquisition system setup, camera calibration and image correction, image-based aircraft localization using instance segmentation, three-dimensional coordinate estimation, and trajectory reconstruction.

5.1. Image Acquisition System Setup

In the proposed approach, two ground-based industrial cameras are employed to form a dual-view observation system for synchronized image acquisition during the aircraft flyover. The image acquisition system comprises two cameras, a network switch, and a host computer. Both cameras are connected to the same switch via Ethernet, while the switch is connected to the host computer to enable synchronized image acquisition and data storage. Basler acA1300-60gc industrial cameras equipped with C23-0824-5M-P lenses are employed in the image acquisition system. This configuration satisfies the basic requirements for imaging a high-speed target in a flyover scenario for three reasons. First, the cameras provide a maximum frame rate of 60 fps, meeting the temporal resolution requirement for trajectory reconstruction during the flyover. Second, the global shutter effectively eliminates rolling distortion and reduces motion blur associated with high-speed target motion. Third, each image frame is assigned a hardware timestamp, enabling unified temporal alignment among the image sequence, the GPS timing reference, and the noise acquisition system. The host computer is also equipped with a GPS timing module to obtain absolute time information and trigger signals, thereby providing a common temporal reference for synchronizing the trajectory and acoustic data.

To maintain spatial consistency between the reconstructed aircraft trajectory and the array-based sound source localization results, trajectory determination is carried out in the same planar coordinate system used for the microphone array. A three-dimensional coordinate system is then established by defining the plane of the inner subarray as the reference plane, with $z = 0$, as illustrated in Figure 8. In the present study, Camera 1 and Camera 2 are positioned approximately at (100, 0, 0) and (100, -100, 0), respectively. Their optical axes are adjusted so that the cameras provide a stable overlapping field of view above the array, covering the primary observation region during the aircraft flyover.

 doi:10.20944/preprints202603.1424.v1

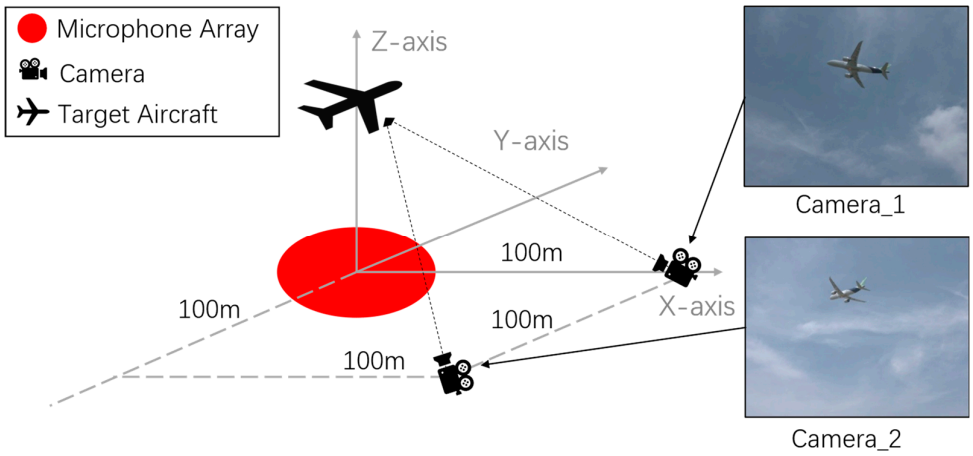

Figure 8. Schematic of the coordinate system.

5.2. Camera Calibration

Because of lens characteristics and manufacturing tolerances, the actual imaging process generally deviates from the ideal pinhole camera model and introduces image distortion. Camera calibration is therefore performed in advance, and the acquired images are subsequently corrected using the calibrated camera parameters. The basic principle is as follows:

Let the homogeneous coordinates of a spatial point in the world coordinate system be defined as

$$\mathbf{P}_w = [X, Y, Z, 1]^T, \tag{1}$$

where X, Y, and Z are the coordinates of the point in the world coordinate system. Let the corresponding homogeneous image coordinates be denoted by

$$\mathbf{p} = [u, v, 1]^T \quad , \tag{2}$$

where u and v are the pixel coordinates of the projected point on the image plane. Under the ideal pinhole imaging model, their relationship can be written as

$$s\mathbf{p} = \mathbf{K}[\mathbf{Rt}]\mathbf{P}_w \quad , \tag{3}$$

where $\mathbf{K}$ is the intrinsic parameter matrix of the camera, containing the focal lengths and principal point coordinates. $\mathbf{R}$ and $\mathbf{t}$ are the rotation matrix and translation vector in the extrinsic parameters, respectively, which describe the orientation and position of the camera relative to the reference coordinate system. To account for lens distortion, radial and tangential distortion terms are further introduced based on the normalized image-plane coordinates (x, y). Let

$$r^2 = x^2 + y^2 \quad , \tag{4}$$

the radial distortion can be expressed as

$$x_r = x(1+k_1r^2+k_2r^4+k_3r^6) \quad , \tag{5}$$

$$y_r = y(1+k_1r^2+k_2r^4+k_3r^6) \quad , \tag{6}$$

where k_1, k_2, k_3 are the radial distortion coefficients. The tangential distortion can be written as

$$x_t = 2p_1xy + p_2(r^2+2x^2) \quad , \tag{7}$$

$$y_t = p_1(r^2+2y^2) + 2p_2xy \quad , \tag{8}$$

 doi:10.20944/preprints202603.1424.v1

where p_1 and p_2 are the tangential distortion coefficients. By combining radial and tangential distortion, the distorted normalized coordinates (x_d, y_d) are obtained as

$$x_d = x_r + x_t = x(1+k_1r^2+k_2r^4+k_3r^6) + 2p_1xy + p_2(r^2+2x^2) \quad , \tag{9}$$

$$y_d = y_r + y_t = y(1+k_1r^2+k_2r^4+k_3r^6) + p_1(r^2+2y^2) + 2p_2xy. \tag{10}$$

The normalized coordinates can then be mapped to the pixel coordinate system through the intrinsic matrix **K**, yielding

$$u = f_x x_d + c_x \quad , \tag{11}$$

$$v = f_y y_d + c_y \quad , \tag{12}$$

where f_x and f_y are the effective focal lengths in the pixel coordinate system, and (c_x, c_y) denotes the principal point.

Based on the imaging and distortion model described above, camera calibration was carried out using Zhang's planar checkerboard method [21]. First, a checkerboard calibration target with known geometric dimensions was imaged from multiple viewing angles to obtain calibration images under different poses. The checkerboard corner points were then detected in each image, and the correspondence between their pixel coordinates and the physical coordinates on the calibration target was established. Finally, the intrinsic parameters, extrinsic parameters, and distortion coefficients were estimated by nonlinear optimization with reprojection error minimization as the objective. Representative calibration images and the corresponding corner detection results are shown in Figure 9.

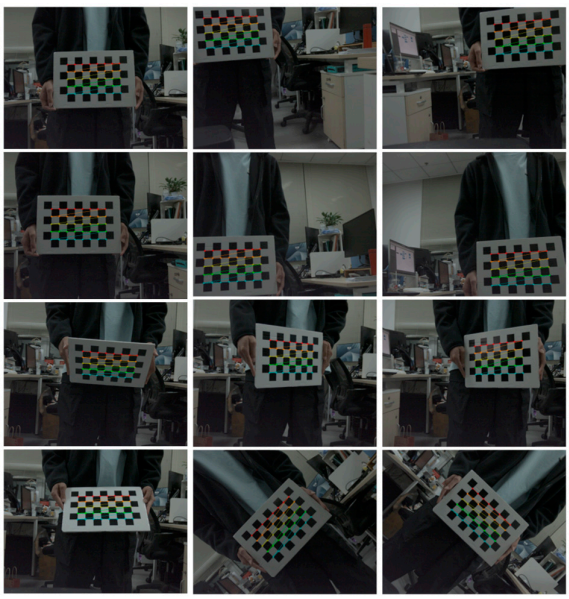

Figure 9. Calibration images and corner extraction results.

After the intrinsic matrix and distortion coefficients were obtained, the raw aircraft images were corrected according to the distortion model described above.

5.3. Image-Plane Localization Using Instance Segmentation

Conventional target detection methods typically represent the target by a bounding box and take its center as the target position. In flyover noise measurement scenarios, however, the predicted bounding box is often unstable due to variations in viewing angle, aircraft attitude, and aircraft configuration. Consequently, the estimated position may deviate from the representative image

 doi:10.20944/preprints202603.1424.v1

position of the aircraft, which in turn degrades the accuracy of subsequent trajectory determination. To overcome this limitation, an instance segmentation method is adopted in this study to extract the aircraft mask, from which the aircraft position in the image plane is determined.

5.3.1. YOLO11 Model

You Only Look Once (YOLO) is employed for aircraft detection and mask extraction [22]. The architecture of YOLO11 is shown in Figure 10. As a single-stage network integrating detection and segmentation, YOLO11 consists of three main components: a backbone, a neck, and a head. The backbone comprises multiple convolutional layers and C3k2 modules for progressively extracting semantic features at different levels. An SPPF (Spatial Pyramid Pooling Fast) module is used to enlarge the receptive field and enhance multi-scale feature representation, while a C2PSA (Cross Stage Partial with Pyramid Squeeze Attention) module is introduced in the high-level feature extraction stage to strengthen the representation of key target regions. The neck performs multi-scale feature fusion through upsampling and feature concatenation, thereby improving the recognition of small targets and targets with scale variations. The head incorporates a segmentation branch and outputs detection and segmentation features at multiple scales, ultimately generating target categories and pixel-level masks for instance-level aircraft recognition and mask extraction. The model maintains detection accuracy while preserving inference efficiency and provides the required region information for subsequent aircraft contour extraction and image-plane localization.

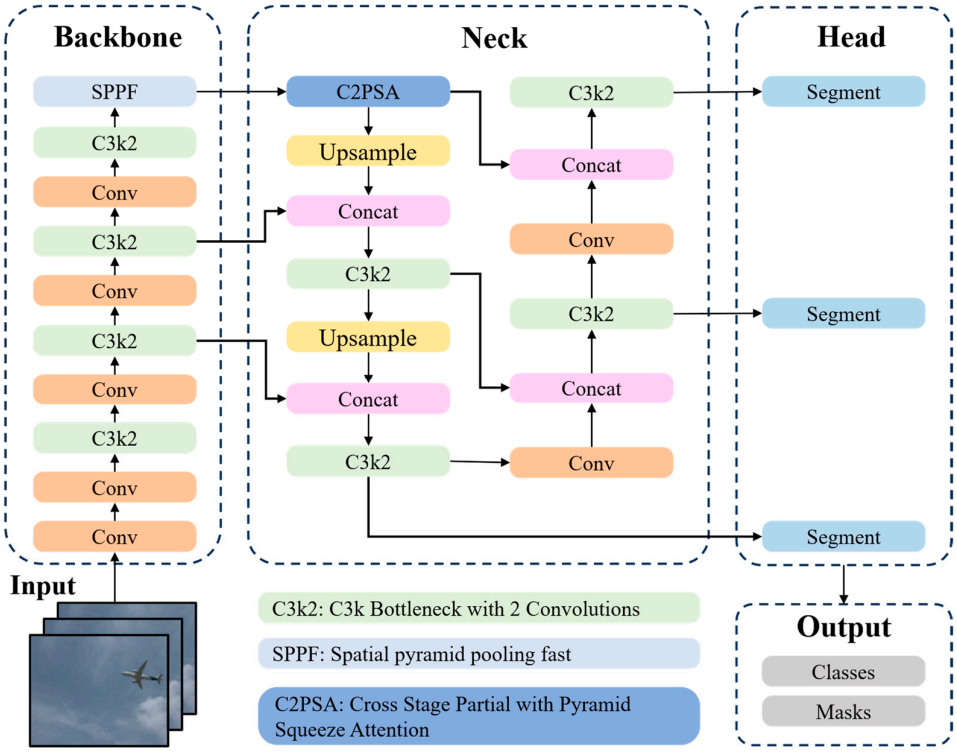

Figure 10. YOLO11 model architecture.

5.3.2. Image Localization

Figure 11 shows the image-plane localization procedure at a given instant using instance segmentation. The raw images from Camera 1 and Camera 2 are first processed by the YOLO11 model to identify the aircraft and extract the corresponding masks. The geometric centroid of each mask is then computed and used as the aircraft position in the image plane for the two cameras at that instant.

 doi:10.20944/preprints202603.1424.v1

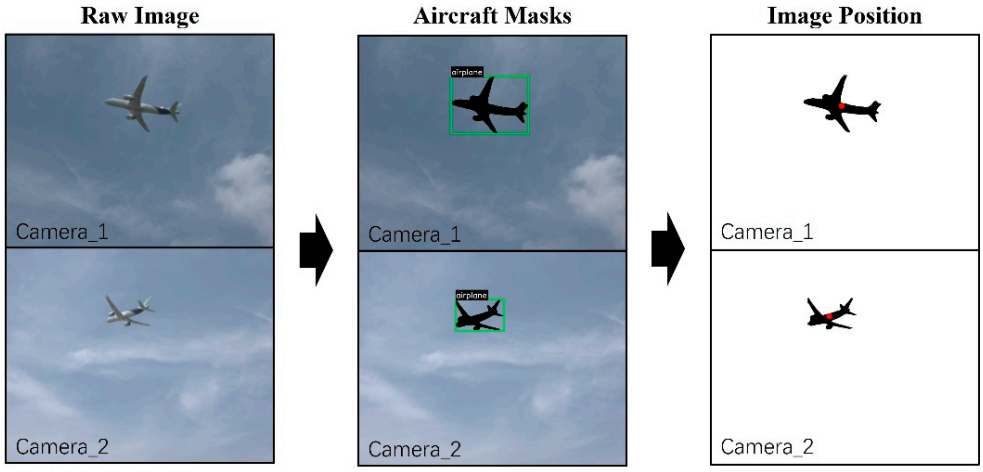

Figure 11. Image-plane localization procedure using instance segmentation.

5.4. 3D Coordinate Estimation and Trajectory Reconstruction

To obtain the continuous spatial position of the aircraft during the flyover, three-dimensional coordinate estimation and trajectory reconstruction are performed based on the observations from two cameras. First, the image-plane coordinates of the aircraft in the two views are combined with the camera extrinsic parameters to estimate the three-dimensional aircraft coordinates in the unified coordinate system through triangulation. Specifically, the target pixel in each view is back-projected, together with the corresponding camera parameters, to form two spatial rays in the common array coordinate system. Under ideal conditions, the intersection of the two rays gives the three-dimensional position of the aircraft. In practice, however, the two rays generally do not intersect exactly because of image-plane localization errors, camera calibration errors, and other uncertainties. Therefore, the closest points on the two rays are determined using the shortest-distance criterion, and their midpoint is taken as the estimated aircraft position. Repeating this procedure for each frame yields a discrete sequence of three-dimensional aircraft coordinates in the unified coordinate system.

Interpolation and smoothing are further applied to the discrete coordinate sequence to reconstruct a continuous flight trajectory. This process reduces frame-to-frame localization jitter and suppresses occasional outliers introduced during image acquisition, thereby improving the continuity and smoothness of the reconstructed trajectory and making it more consistent with the actual aircraft motion.

Figure 12 illustrates the three-dimensional coordinate estimation process and the resulting trajectory reconstruction in the unified coordinate system. The dashed lines indicate the corresponding rays, and the blue curve shows the reconstructed aircraft trajectory. The reconstructed trajectory is continuous and smooth over the observation interval and provides a continuous estimate of the aircraft motion in the unified coordinate system.

 doi:10.20944/preprints202603.1424.v1

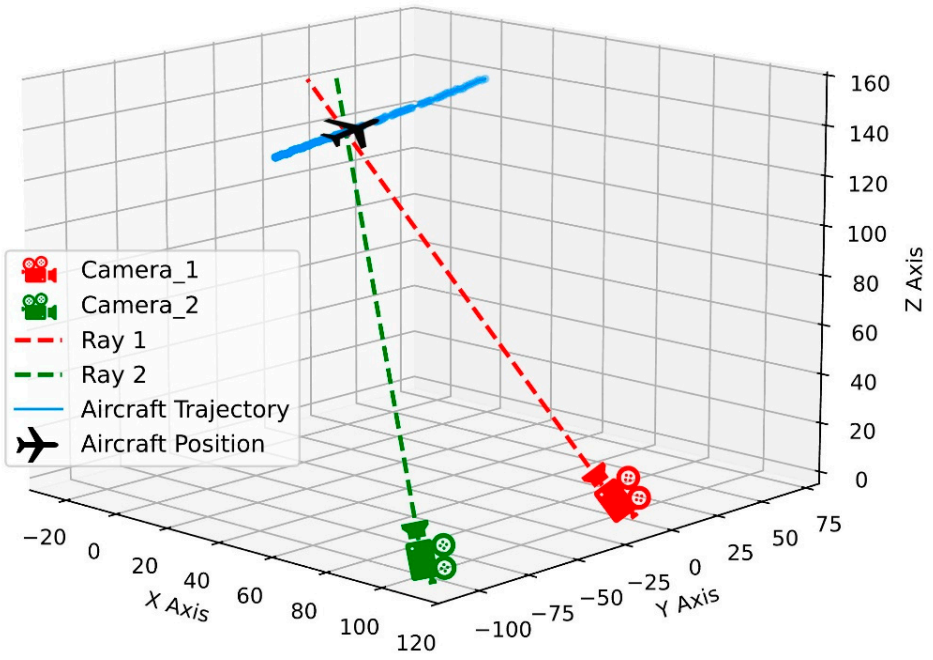

Figure 12. 3D coordinate estimation and trajectory reconstruction results.

5.5. Error Analysis

The accuracy of the reconstructed aircraft trajectory was quantitatively evaluated using flight altitude and speed data. The results indicate that the reconstructed trajectory achieves meter-level accuracy and is sufficiently stable for subsequent sound source localization. As shown in Figure 13 and **Figure 14**, the estimated altitude and speed exhibit temporal variations that are generally consistent with those of the reference data.

Further statistical error analysis indicates that, for altitude estimation, the mean error is 0.86 m, the root mean square error (RMSE) is 0.95 m, and the mean absolute percentage error (MAPE) is 0.65%. For speed estimation, the mean error is 2.10 m/s, the RMSE is 2.19 m/s, and the MAPE is 2.35%. These results indicate that the proposed method achieves meter-level trajectory estimation accuracy and provides stable trajectory reconstruction estimates for subsequent sound source localization.

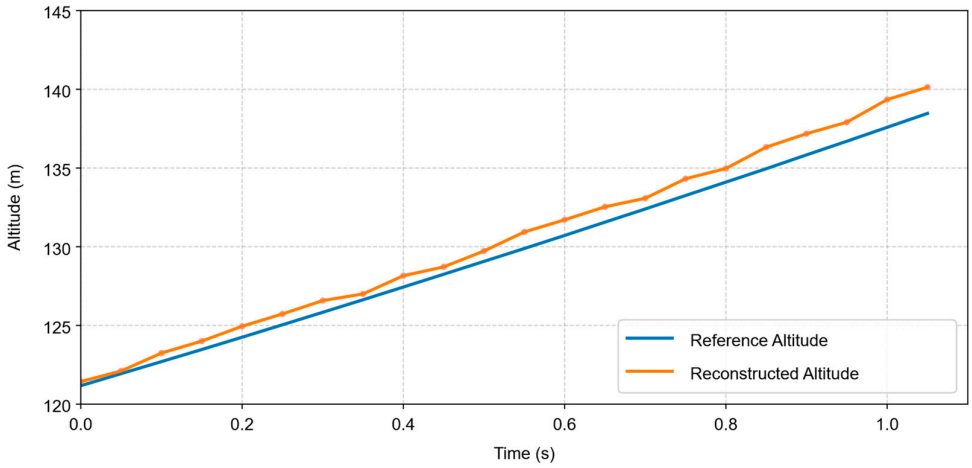

Figure 13. Comparison between measured altitude and reference altitude.

 doi:10.20944/preprints202603.1424.v1

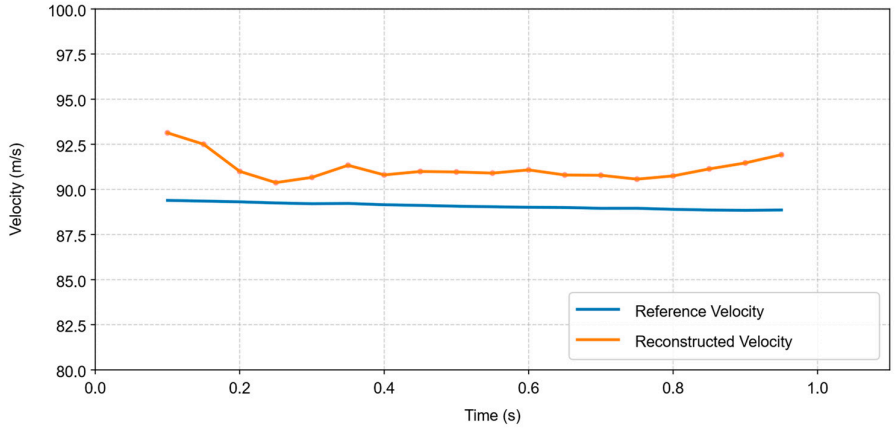

Figure 14. Comparison between measured velocity and reference velocity.

6. Data Processing

6.1. The MCB-GT Algorithm

The Modal Composition Beamforming for General Trajectory (MCB-GT) algorithm proposed by Zhang is adopted for sound source localization in aircraft flyover measurements [23]. This algorithm extends the Modal Composition Beamforming (MCB) principle from rotating-source localization to the localization of sources undergoing general motion [24]. A frequency-domain modal representation of the sound field generated by a generally moving source is established, on the basis of which the MCB-GT algorithm is formulated. Compared with conventional beamforming methods based on fixed propagation-delay phase compensation, MCB-GT can more appropriately characterize the Doppler effect induced by source motion and the time-varying propagation geometry during flyover, thereby improving the applicability of beamforming to moving sound sources.

Assume that the array consists of M microphones, and let the position of the m-th microphone be denoted by $\mathbf{x}_m$ $(m = 1,2, \dots, M)$. Let $\mathbf{y}_s$ denote the position vector of the s-th scan point, and ω be the target angular frequency. Then, at the shifted frequency $\omega + \Delta\omega$, the received spectrum at the array microphones can be written as

$$\tilde{p}(\mathbf{x}_m, \omega + \Delta\omega) = \tilde{q}_s(\omega)\, \mathcal{F}_{\Delta\omega}\left[G_{\omega+\Delta\omega}(r_{m,s}(\tau))\right] \quad , \tag{13}$$

where $\tilde{q}_s(\omega)$ is the spectrum of the equivalent source at the scan point and angular frequency ω, $G_{\omega+\Delta\omega}(\cdot)$ is the free-field Green's function, $r_{m,s}(\tau)$ is the instantaneous propagation distance from the source trajectory to the microphone, and $\mathcal{F}_{\Delta\omega}(\cdot)$ denotes the Fourier transform evaluated at the frequency shift $\Delta\omega$.

For a microphone signal containing N sampled points over a sampling duration T, the frequency resolution is $2\pi/T$. Let m_0 denote the shifted modal order. The microphone signal in the time domain can then be written as the superposition of a series of discrete modes:

$$p(\mathbf{x}_m, t) = \tilde{q}_s(\omega) \sum_{m_0=-N/2}^{N/2-1} a_{m_0}(\mathbf{x}_m, \mathbf{y}_s, \omega)\, e^{i\left(\omega + m_0 \frac{2\pi}{T}\right)t} \quad , \tag{14}$$

where $a_{m_0}(\mathbf{x}_m, \mathbf{y}_s, \omega)$ is the transfer function of the m_0-th shifted mode, defined as

$$\tilde{p}\left(\mathbf{x}_m, \omega + m_0 \frac{2\pi}{T}\right) = \tilde{q}_s(\omega)\, a_{m_0}(\mathbf{x}_m, \mathbf{y}_s, \omega) \, , \tag{15}$$

which further gives

$$a_{m_0}(\mathbf{x}_m, \mathbf{y}_s, \omega) = \mathcal{F}_{m_0 \frac{2\pi}{T}}\left(G_{\omega + m_0 \frac{2\pi}{T}}\left(r_{m,s}(\tau)\right)\right) \quad . \tag{16}$$

 doi:10.20944/preprints202603.1424.v1

Accordingly, the transfer function of each shifted mode can be calculated directly from the microphone position calibration results and the aircraft trajectory determination results.

Based on the principle of modal composition localization, the beamforming output of MCB-GT can be expressed as

$$B(s,\omega)=\frac{1}{M}\left|\sum_{m=1}^{M}\sum_{m_0=-\frac{M_0}{2}}^{\frac{M_0}{2}-1}a_{m_0}^{*}\left(\mathbf{x}_m,\mathbf{y}_s,\omega\right)\tilde{p}\left(\mathbf{x}_m,\omega+m_0\frac{2\pi}{T}\right)\right|^2 \quad , \tag{17}$$

where $B(s,\omega)$ denotes the beamforming output at the s-th scan grid point and imaging angular frequency ω, M_0 denotes the total number of modes, and $(\cdot)^*$ denotes complex conjugation. A larger value of M_0 generally leads to more accurate localization, but also increases the computational cost. To balance computational efficiency and shifted-frequency coverage, M_0 can be selected according to the maximum aircraft speed relative to the array, denoted by v_s, within the sampling window, generally satisfying

$$\frac{M_0}{2}\frac{2\pi}{T}\geq \mathrm{round}\left(\alpha\frac{c}{c-v_s}\omega\right) \quad , \tag{18}$$

where α is a coefficient greater than 1, with a recommended value of 1.2, and $\mathrm{round}(\cdot)$ denotes the rounding operation.

Overall, the MCB-GT algorithm exploits the shifted modal information associated with moving sound sources and provides an effective signal-processing framework for sound source localization in aircraft flyover measurements, thereby laying the foundation for subsequent high-resolution source identification.

6.2. Sound Source Localization Results

The practical applicability of the proposed flyover noise measurement procedure was demonstrated by applying the MCB-GT algorithm described above to flyover test data acquired during the approach of a large civil aircraft and performing sound source localization imaging.

Figure 15 presents the sound source localization results for the one-third-octave band centered at 1.8 kHz. The map is shown using the same color scale, with the aircraft geometric outline superimposed as a spatial reference. The dominant noise sources are mainly distributed around the landing gear, engines, and flaps, consistent with the typical source distribution characteristics of aircraft flyover noise during the approach phase.

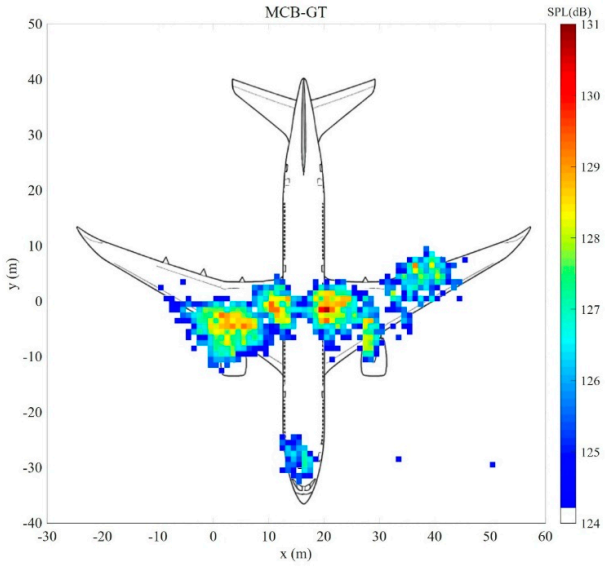

Figure 15. One third octave sound source localization result at a center frequency of 1800 Hz.

 doi:10.20944/preprints202603.1424.v1

More specifically, the results not only identify three prominent landing-gear noise sources, but also clearly distinguish the source distribution in the main landing-gear region from that in the engine region. In addition, a relatively distinct noise concentration is observed near the flap on the left side of the aircraft. This feature may be associated with asymmetry in the flight attitude or with local aerodynamic loading. These results demonstrate that the proposed procedure can provide effective and physically interpretable sound source localization results, and is therefore suitable for aircraft flyover measurements of large civil aircraft.

7. Discussions

The discussions are given in this section. Sentences written in italics at the beginning of each paragraph guide the discussion in each paragraph.

Why was a straight-arm design adopted for the outer subarray instead of a spiral array? The microphone array was designed by considering both localization performance and field deployment efficiency. Although spiral arrays usually provide superior imaging performance, they are less convenient for deployment in large outdoor measurements. Therefore, the inner subarray was designed with a spiral layout to ensure good localization performance at mid and high frequencies. In contrast, the outer subarray adopted a straight-arm layout, which is more suitable for modular assembly, transportation, and repeated installation, and is therefore more practical for aircraft flyover measurements.

Do computer-vision methods improve the efficiency and accuracy of aircraft flyover measurements? Yes. Computer-vision methods improve the efficiency of aircraft flyover measurements while maintaining the required accuracy. They can be used for rapid coordinate calibration of large-scale microphone arrays and for aircraft trajectory reconstruction, thereby reducing manual effort and improving the automation of flight-parameter acquisition. Their main role is to sufficiently accurate geometric inputs for sound source localization, while greatly reducing manual effort in large-scale tests.

Does the installation of ground-board mounted microphones affect sound source localization results? It is likely to affect sound source localization results. Different installation conditions may influence signal consistency across microphones and further affect the reliability of source localization [25]. Existing studies have mainly focused on the quantitative effects of such factors on sound pressure level measurements. However, how these installation-related factors further affect sound source localization results has not yet been sufficiently investigated.

Why was the MCB-GT algorithm adopted in this study? Because it is more consistent with the physical characteristics of aircraft flyover. Compared with the conventional strategy of Doppler correction followed by beamforming, it can more directly account for the time-varying propagation geometry and Doppler effect caused by aircraft motion. It is therefore theoretically more suitable for moving sound source localization in aircraft flyover measurements. However, its performance still depends on parameter settings such as the modal number. Since different algorithms may behave differently under different conditions, this issue will be further investigated in future work.

8. Conclusions

This study presents an integrated procedure for aircraft flyover measurements of large civil aircraft developed in China, covering microphone array design, installation and calibration, noise acquisition system setup and data acquisition, aircraft trajectory determination, and data processing. The procedure is intended to improve the efficiency of outdoor measurements while ensuring the reliability of the key parameters required for flyover noise source localization. Two computer-vision-based techniques are integrated into the procedure. A vision-based microphone position calibration method is developed to enhance field deployment efficiency while preserving microphone positional accuracy. In addition, dual-camera-based trajectory determination method incorporating instance segmentation is established, and the reconstructed trajectory provides sufficient accuracy for sound source localization.

 doi:10.20944/preprints202603.1424.v1

The proposed procedure is validated using flyover noise test data obtained during the approach phase of a domestically developed large civil aircraft. The results demonstrate its practical applicability in real measurement scenarios. This work provides a useful methodological reference for future aircraft flyover measurements and sound source localization studies.

Acknowledgements: This work is supported by the National Natural Science Foundation of China (W2442003).

Abbreviations

The following abbreviations are used in this article:

ICAO	International Civil Aviation Organization
DLR	German Aerospace Center
ONERA	French Aerospace Lab
NASA	National Aeronautics and Space Administration
QTD	Quiet Technology Demonstrator
CAAC	Civil Aviation Administration of China
GPS	Global Positioning System
NI	National Instruments
YOLO	You Only Look Once
SPPF	Spatial Pyramid Pooling Fast
C2PSA	Cross Stage Partial with Pyramid Squeeze Attention
MCB-GT	Modal Composition Beamforming for General Trajectory
MCB	Modal Composition Beamforming
RMSE	Root Mean Square Error
MAPE	Mean Absolute Percentage Error

References

1. International Civil Aviation Organization (ICAO). Annex 16 to the Convention on International Civil Aviation, Volume I—Aircraft Noise (Environmental Protection); ICAO: Montreal, QC, Canada, 2017.
2. Electronic Code of Federal Regulations (e-CFR). 14 CFR Part 36—Noise Standards: Aircraft Type and Airworthiness Certification. Available online: https://www.ecfr.gov/current/title-14/chapter-I/subchapter-C/part-36 (accessed on 3 March 2026).
3. Michel, U.; Helbig, J.; Barsikow, B.; Hellmig, M.; Schuettpelz, M. Flyover noise measurements on landing aircraft with a microphone array. In Proceedings of the 4th AIAA/CEAS Aeroacoustics Conference, Toulouse, France, 2–4 June 1998. https://doi.org/10.2514/6.1998-2336.
4. Michel, U.; Qiao, W. Directivity of landing-gear noise based on flyover measurements. In Proceedings of the 5th AIAA/CEAS Aeroacoustics Conference and Exhibit, Bellevue, WA, USA, 10–12 May 1999; AIAA Paper 1999-1956. https://doi.org/10.2514/6.1999-1956.
5. Qiao, W.; Michel, U. Experimental study of airframe noise with improved data reduction method of microphone array measurements (in Chinese). Acta Aeronaut. Astronaut. Sin. 2008, 29, 527–533. https://doi.org/10.3321/j.issn:1000-6893.2008.03.002.
6. Stoker, R.; Guo, Y.; Streett, C.; Burnside, N. Airframe noise source locations of a 777 aircraft in flight and comparisons with past model-scale tests. In Proceedings of the 9th AIAA/CEAS Aeroacoustics Conference and Exhibit, Hilton Head, SC, USA, 12–14 May 2003.
7. Elkoby, R.; Brusniak, L.; Stoker, R.; Khorrami, M.R.; Abeysinghe, A.; Moe, J.W. Airframe noise test results from the QTD II flight test program. In Proceedings of the 13th AIAA/CEAS Aeroacoustics Conference, Rome, Italy, 21–23 May 2007.
8. Piet, J.F.; Michel, U.; Böhning, P. Localization of the acoustic sources of the A340 with a large phased microphone array during flight tests. In Proceedings of the 8th AIAA/CEAS Aeroacoustics Conference and Exhibit, Breckenridge, CO, USA, 17–19 June 2002.
9. Guérin, S.; Michel, U.; Siller, H.; Finke, U.; Saueressig, G. Airbus A319 database from dedicated flyover measurements to investigate noise abatement procedures. In Proceedings of the 11th AIAA/CEAS Aeroacoustics Conference, Monterey, CA, USA, 23–25 May 2005.

 doi:10.20944/preprints202603.1424.v1

10. Blais, J.F.; Camier, C.; Patenaude-Dufour, M.; Lesage, J.; Gauthier, P.A.; Berry, A. Fly-over aircraft noise measurement campaign at Montreal-Trudeau airport using a microphone array. Proc. Meet. Acoust. 2013, 19, 055084. https://doi.org/10.1121/1.4800879.
11. Wong, J.W.; Nesbitt, E.H.; Jones, M.G.; Nark, D.M. Flight test methodology for NASA advanced inlet liner on 737MAX-7 test bed (Quiet Technology Demonstrator 3). In Proceedings of the 25th AIAA/CEAS Aeroacoustics Conference, Delft, The Netherlands, 20–23 May 2019; AIAA Paper 2019-2763. https://doi.org/10.2514/6.2019-2763.
12. Siller, H.A.; Schumacher, T.; Hage, W. Low noise ATRA—Phased array measurements of jet noise in flight. In Proceedings of the AIAA AVIATION 2021 FORUM, Virtual, 2–6 August 2021; AIAA Paper 2021-2160. https://doi.org/10.2514/6.2021-2160.
13. Lincke, D.; Schumacher, T.; Pieren, R. Evaluation of microphone array methods for aircraft flyover measurements: Development of a virtual test environment. In Fortschritte der Akustik—DAGA 2022; DEGA: Stuttgart, Germany, 2022; pp. 781–783. Available online: https://pub.dega-akustik.de/DAGA_2022/data/articles/000114.pdf (accessed on 17 December 2025).
14. Czech, M.J.; Thomas, R.H.; Guo, Y.; June, J.C.; Clark, I.A.; Shoemaker, C.M. Propulsion airframe aeroacoustics and aircraft system noise flight test on the ecoDemonstrator 2020—Boeing 787 testbed aircraft. In Proceedings of the 28th AIAA/CEAS Aeroacoustics Conference, Southampton, UK, 14–17 June 2022; AIAA Paper 2022-2994.
15. Chen, T.; Hou, H.; Chen, Z.; Wang, Y.; Li, X. ARJ aircraft noise measurement from fly-over test (in Chinese). Acta Metrol. Sin. 2012, 33, 437–440. https://doi.org/10.3969/j.issn.1000-1158.2012.05.12.
16. Chen, T.; Hou, H.; Chen, Z. ARJ aircraft landing gear noise characteristics from fly-over measuring (in Chinese). J. Vib. Shock 2012, 31, 83–86.
17. Chen, T.; Hou, H.; Chen, Z.; Wang, Y.; Li, X. Landing gear noise identification in the ARJ21 aircraft during landing stage (in Chinese). Acta Acust. 2013, 38, 615–623. https://doi.org/10.15949/j.cnki.0371-0025.2013.05.012.
18. Underbrink, J.R. Aeroacoustic phased array testing in low speed wind tunnels. In Aeroacoustic Measurements; Mueller, T.J., Ed.; Springer: Berlin/Heidelberg, Germany, 2002; pp. 98–217. https://doi.org/10.1007/978-3-662-05058-3_3.
19. Underbrink, J.R. Pletharrays for aeroacoustic phased array applications. Int. J. Aeroacoust. 2017, 16, 202–229. https://doi.org/10.1177/1475472X17718884.
20. Tao, S.; Lee, C.W.; Ma, W. Sound source localization errors caused by installation deviations of large-scale microphone arrays. Aerosp. Syst. 2025. https://doi.org/10.1007/s42401-025-00363-z.
21. Zhang, Z. A flexible new technique for camera calibration. IEEE Trans. Pattern Anal. Mach. Intell. 2000, 22, 1330–1334. https://doi.org/10.1109/34.888718.
22. Ultralytics. YOLO11. Available online: https://docs.ultralytics.com/models/yolo11/ (accessed on 3 March 2026).
23. Zhang, C. Key Theoretical Research on Array Imaging Method for Moving Sound Source Localization (in Chinese). Ph.D. Thesis, Shanghai Jiao Tong University, Shanghai, China, 2025.
24. Zhang, C.; Ma, W. Frequency-domain expression of sound pressure field radiated by monopole source with general moving trajectory. J. Sound Vib. 2024, 570, 118137. https://doi.org/10.1016/j.jsv.2023.118137.
25. Go, S.T.; Kingan, M.J.; Schmid, G.; Hall, A. On the use of ground-board mounted microphones for outdoor noise measurements. J. Sound Vib. 2024, 584, 118432. https://doi.org/10.1016/j.jsv.2024.118432.